



Polaron formation in Bi-deficient BaBiO 3

W. Román Román Acevedo, S Di Napoli, F. Romano, G Rodríguez Ruiz, P. Nukala, C. Quinteros, J. Lecourt, Ulrike Luders, V. Vildosola, D. Rubi

► To cite this version:

W. Román Román Acevedo, S Di Napoli, F. Romano, G Rodríguez Ruiz, P. Nukala, et al.. Polaron formation in Bi-deficient BaBiO 3. *Physical Review B*, 2021, 104 (12), pp.125307. 10.1103/PhysRevB.104.125307 . hal-03433504

HAL Id: hal-03433504

<https://hal.science/hal-03433504>

Submitted on 17 Nov 2021

HAL is a multi-disciplinary open access archive for the deposit and dissemination of scientific research documents, whether they are published or not. The documents may come from teaching and research institutions in France or abroad, or from public or private research centers.

L'archive ouverte pluridisciplinaire **HAL**, est destinée au dépôt et à la diffusion de documents scientifiques de niveau recherche, publiés ou non, émanant des établissements d'enseignement et de recherche français ou étrangers, des laboratoires publics ou privés.

Polaron formation in Bi-deficient BaBiO₃

W. Román Acevedo,^{1,2} S. Di Napoli,^{1,2} F. Romano,^{1,2} G. Rodríguez Ruiz,^{1,2} P. Nukala,^{3,4} C. Quinteros,⁴ J. Lecourt,⁵ U. Lüders,⁵ V. Vildosola,^{1,2} and D. Rubí^{1,2}

¹Departamento de Física de la Materia Condensada, GIyA-CNEA,
Av. General Paz 1499, (1650) San Martín, Pcia. de Buenos Aires, Argentina

²Instituto de Nanociencia y Nanotecnología (INN CNEA-CONICET), 1650 San Martín, Argentina

³Center for Nanoscience and Engineering, Indian Institute of Science, Bangalore, 560012, India

⁴Zernike Institute for Advanced Materials, University of Groningen, The Netherlands

⁵CRISMAT, CNRS UMR 6508, ENSICAEN, 6 Boulevard Maréchal Juin, F-14050 Caen Cedex 4, France

BaBiO₃ is a charged ordered Peierls-like perovskite well known for its superconducting properties upon K or Pb doping. We present a study on the transport and electronic properties of BaBiO₃ perovskite with strong Bi-deficiency. We show that it is possible to synthesize BaBiO₃ thin layers with Bi-vacancies above 8-10% by depositing an yttrium-stabilized zirconia capping layer. By combining transport measurements with *ab initio* calculations we propose a scenario where the Bi-vacancies give rise to the formation of polarons and suggest that the electrical transport is dominated by the migration of these polarons trapped at Bi³⁺ sites. Our work shows that cation vacancies engineering -hardly explored to date- appears as a promising pathway to tune the electronic and functional properties of perovskites.

PACS numbers:

I. INTRODUCTION

Perovskite oxides display a plethora of physical properties, such as magnetism¹, ferroelectricity² and/or superconductivity³, making them attractive materials for the development of sensing⁴, information storage⁵ or computing⁶ devices, among others. The possibility of implementing these devices has boosted in the last decades as oxide thin films and heterostructures with excellent crystalline properties, chemistry and atomically controlled surfaces and interfaces have been developed. Defects are ubiquitously found in oxide thin films, oxygen vacancies being the most common ones⁷. Cationic vacancies have been less studied due to their lower concentration in comparison with oxygen vacancies⁸, but they might have a significant impact on the physical properties of the films as they could strongly modify the oxide electronic structure.

BaBiO₃ (BBO) is a perovskite which becomes superconducting upon Pb or K doping^{9,10} with high critical temperatures up to ~ 30 K. Pristine BBO is an insulator due to the existence of a charge ordered state comprising Bi ions with formal +3 and +5 valences¹¹. This is accompanied with structural distortions involving both the so-called breathing distortions and tiltings of BiO₆ octahedra¹², which reduces the high temperature cubic crystal symmetry to a monoclinic structure at room temperature. Bi-O bond distances have been reported as 2.11 and 2.29 Å, respectively¹². Spectroscopic experiments have failed to resolve valence differences between Bi ions in both crystallographic sites^{13,14}, while theoretical work suggests a common $\approx +3$ state, which has been rationalized in terms of spatially extended Bi-O bonds related to hybridized Bi-6s and O-2p atomic orbitals¹⁵⁻¹⁷. BBO has been proposed to behave as a topological insulator upon electron doping¹⁸, and it was also theoretically sug-

gested to present a 2D electron gas in its Bi-terminated (001) surface¹⁹. Moreover, 2D superconductivity has been shown at the BBO/BaPbO₃ interface^{20,21}. Reports on BBO thin films are scarce²²⁻³¹. Most works report on the growth and properties of BBO on SrTiO₃ (STO) substrates^{22,23,25,28-31}, with both materials presenting a rather large lattice mismatch of $\approx 12\%$. It was shown that this misfit is accommodated through the formation of an ultrathin interfacial δ-Bi₂O₃ layer with a fluorite structure, which forms a coherent interface with the substrate and a semi-coherent interface with BBO^{28,31}. Recent reports indicate that the electronic structure of BBO on STO is thickness dependent and is affected by chemical and structural effects imposed by the substrate/film interface^{29,32}. These results indicate that substrate effects on the BBO electronic structure might not be disregarded in thin epitaxial films.

With the aim of studying the effect of (B-site) Bi deficiency on the electronic and transport properties of BBO, we have developed a fabrication procedure allowing for the introduction of a large amount of Bi vacancies in stoichiometric BBO thin films on silicon. From a combination of experiments and *ab initio* calculations, it is proposed that Bi deficiency leads to the formation of polarons that dominate the electrical transport. Our work shows the control of cation deficiency as an emerging degree of freedom that allows tuning the BBO electronic structure and its functional properties.

II. EXPERIMENTAL SECTION

BBO thin films were deposited by pulsed laser deposition using a Nd-YAG Spectra Physics laser with $\lambda = 266$ nm and 850 mJ per pulse. Structural characterization

of the films was performed by means of X-ray diffraction (XRD) using two Panalytical Empyrean diffractometers with PIXcel ultrafast detectors, in standard Bragg-Brentano configuration (0.02° steps were used for 2θ scanning). Transmission electron microscopy (TEM) was performed with a Thermo Fisher Scientific Themis Z monochromated and double corrected microscope operated at 300 kV.

In order to get Bi-deficient BBO, we followed this procedure: first, we deposited a stoichiometric BBO film (≈ 165 nm thick) on commercial Si/SiO₂ substrate, at a temperature and oxygen pressure of 550 °C and 0.01 mbar, respectively. We chose this substrate in order to obtain strain-free polycrystalline films, as will be shown below. Next, we deposited (in-situ), on top of BBO, a yttrium stabilized zirconia (YSZ, ≈ 17 nm thick) capping layer, at room temperature, at an optimized oxygen pressure of 0.1 mbar. YSZ is a well known oxygen conductor³³ but has also been reported to display high cationic conductivities³⁴. In our case, under the proper deposition conditions, YSZ capping favours the diffusion of Bi from BBO to YSZ, leading to an interfacial BBO layer with a strong Bi deficiency.

Figure 1(a) shows X-ray diffraction spectra recorded for both bare and capped BBO films. It is found in both cases the presence of peaks corresponding to the BBO perovskite structure while, for capped BBO, YSZ remains amorphous. BBO peaks were indexed considering a pseudo-cubic (PC) lattice. We extracted a cell parameter for bare BBO $a_{PC} = 4.339(5)$ Å, in excellent agreement with the value corresponding to bulk BBO (4.335 Å). Upon YSZ capping, there is a shift of X-ray peaks towards lower angles (see Figure 1(b)), reflecting an (average) BBO unit cell parameter expansion of $\approx 0.5\%$. This is a first indication of the formation of Bi vacancies at the BBO layer, as unit cell enlargement is a signature of B-site vacancies in perovskites³⁶⁻³⁸. We will come back later to this issue.

Figure 1(e) displays a HAADF-STEM cross-section of a capped BBO film. First we notice the existence of a thin BaO layer (≈ 11 nm, non detectable by XRD) at the substrate/BBO interface, confirmed by the EDS maps displayed at the Suppl. Information³⁵. This interfacial BaO layer has been observed before in BBO thin films²⁷ and can be related to the poor sticking coefficient of Bi ions during the first growth stages^{29,39}. Next, Figure 1(c) displays a BBO layer divided in two zones with different contrast, the darker one (≈ 30 nm thick) located at the interface with YSZ. As HAADF brightness is higher for species with high atomic number such as Bi, the darker BBO fringe is an indication of Bi-deficiency at this zone. We notice that it is difficult to perform a precise composition quantification, as during EDS mapping we observed some grain growth together with changes in the HAADF contrast between BBO and Bi-deficient BBO³⁵, indicating atomic diffusion during the measurement. With this constraint in mind,

we can roughly estimate a lower bound of $\approx 8\text{-}10\%$ of Bi vacancies at the Bi-deficient BBO layer³⁵. This statement is supported from the analysis of (200)_{PC} X-ray peaks performed in the Suppl. Information³⁵. The (200)_{PC} reflection of bare BBO can be fitted with a single Gaussian component, centered at $2\theta = 41.59^\circ$, corresponding to a bulk-like cell parameter 4.339(5) Å. On the other hand, the capped BBO (200)_{PC} reflection shows a broadened peak with a slight asymmetry. The peak can be deconvoluted by assuming two Gaussian contributions centered at $2\theta = 41.59^\circ$ and $2\theta = 41.25^\circ$. These two components are attributed to BBO and Bi-deficient BBO, with cell parameters 4.339(5) Å and 4.374(5) Å, respectively. The latter cell parameter accounts for a ≈ 4 pm BBO cell expansion due to the presence of Bi-vacancies. We recall that in the case of Ti deficient SrTiO₃ such expansion corresponds to a 10-15% B-cation deficiency³⁶, allowing an additional estimation of the amount of B-site vacancies in the Bi-deficient layer of capped BBO, which is consistent with the previous one obtained from microscopy analysis.

Now we will focus on the electrical transport properties of our samples. BBO single crystals were reported to display an insulating, thermally activated behavior⁴⁰. Transport properties in BBO thin films have been rarely published: some authors reported an "insulating behavior"²⁴ in BBO thin films on MgO but no temperature dependent resistivity was shown, while a negative resistance coefficient, in the range 200-300 K, was displayed for BBO films on silicon²⁶. We recall that the transport properties in semiconducting oxide thin films can be highly affected by the presence of defects. For instance, BaSnO₃ thin films were shown to present dramatic changes in their resistivity values -and the corresponding temperature behavior- depending on the films' free carriers concentration⁴¹, strongly linked to the type and number of existing defects.

Electrical transport has been measured on the deposited structures at low temperatures (50-200 K) in a 4-point configuration using a multipurpose Quantum Design Versalab cryostat. In order to gain electrical access to the capped BBO samples, we have covered some parts of the substrate by shadows masks during the deposition (Figure 2(b)). Electrical contacts were fixed with silver paste. Figure 2(c) displays the evolution of the 4-points resistance versus temperature for both uncapped and capped BBO films. Bare BBO films show a resistance nearly independent of the temperature -in the measured temperature range-, indicating that the expected thermally activated behavior (negative resistance coefficient) is compensated with a reduction of carriers mobility as temperature increases. We note that the mentioned behavior of the mobility with temperature implies that mobility is limited by phonons rather than by impurity scattering, this balance being very sensitive to free carriers density⁴². On the other hand, capped BBO shows lower resistance values -a 6-fold decrease at 175 K- together

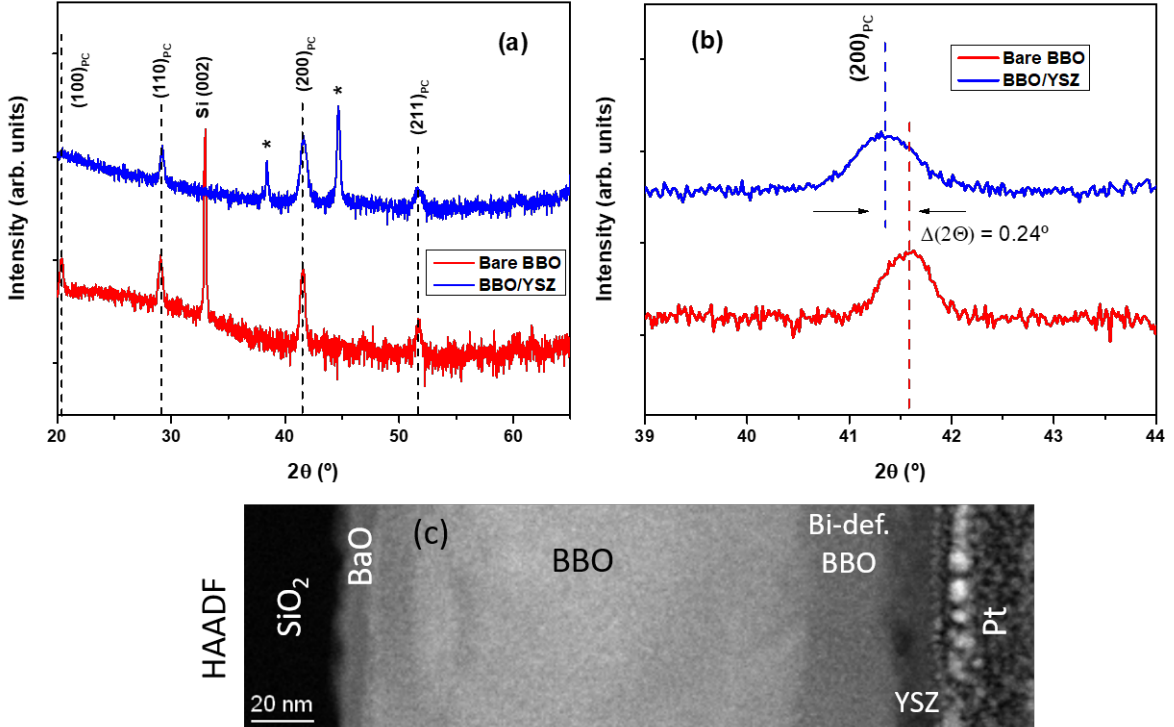


FIG. 1: (a) X-ray diffraction spectra corresponding to both bare and capped BBO. Peaks indexes correspond to the pseudo-cubic (PC) perovskite BBO lattice. Peaks marked with * correspond to the sample holder used for the measurement of the capped BBO sample³⁵. Zero-shift corrections were made from the position of Si peaks; (b) Blow-up of the spectra displayed in (a), evidencing the shift of diffraction peaks to lower angles for capped BBO. Maxima are shifted by 0.24 °. Also, capped BBO displayed broader diffraction peaks (FWHM of ≈ 0.5 ° and ≈ 0.7 ° for BBO and capped BBO, respectively) with a slight asymmetry; (c) TEM HAAADF image corresponding to a BBO/YSZ bilayer on Si/SiO₂, with the YSZ grown at an oxygen pressure of 0.1mbar. The Pt layer on top of the YSZ layer was deposited for the lamella preparation.

with a semiconducting-like behavior characterized by a decrease of the resistance as the temperature increases. We checked in separated control experiments that both SiO₂ and YSZ present resistances several orders of magnitude higher than those shown in Figure 2(c) and this is also the case for the estimated resistance corresponding to the BaO layer (> 10 GΩ), given its reported resistivity ($\approx 10^4 \Omega\text{cm}$ at ≈ 700 °C) and semiconducting-like temperature behavior⁴³. Therefore we can safely exclude the contribution of these three layers to the electrical transport and assume that, for capped BBO, the electrical transport flows through two parallel channels related to BBO and Bi-deficient BBO layers (see the sketch of Figure 2(a)). This scenario was considered to fit the experimental data by proposing an equivalent circuit formed by a temperature independent resistance R_{BBO} for the BBO layer in parallel with a polaronic transport channel, attributed to the Bi-deficient BBO layer, with a temperature dependent resistance $R_{Pol}(T)$ given by⁴⁴

$$R_{Pol}(T) = \frac{K_0 a}{g_d e^2 \nu_0} k_B T \exp\left(\frac{E_\sigma}{k_B T}\right), \quad (1)$$

where k_B is the Boltzmann constant, T is the absolute temperature, e is the electronic charge, a is the polaron hopping distance, ν_0 is the jump attempt frequency - related to the phonon vibrations coupled to the polaron -, E_σ is the activation energy for polaron hopping, g_d is an adimensional factor that depends on the hopping geometry⁵⁸ and $K_0=L/Wt$, with L , W and t being the length, width and thickness of the Bi-deficient BBO layer, respectively.

The $R(T)$ for the bilayer is thus given by

$$R(T) = \frac{R_{BBO} R_{Pol}(T)}{R_{BBO} + R_{Pol}(T)}. \quad (2)$$

The fitting of $R(T)$ is shown with a red full line in Figure 2(c) and displays a reasonable agreement with the experimental data for $E_\sigma=0.12$ eV and $K_0 \frac{a k_B}{g_d e^2 \nu_0} = 5.0 \Omega/K$.

If we take $\nu_0=1.710^{13}$ Hz (the breathing mode vibration frequency⁴⁵) , $a=0.437\text{nm}$ -corresponding to this perovskite cell parameter-, $g_d=3/8$ ⁵⁹ and $K_0=0.067 \text{ nm}^{-1}$ ($L/W \approx 2$ given by our sample geometry and $t=30 \text{ nm}$, as extracted from the TEM analysis of Figure 1) we ob-

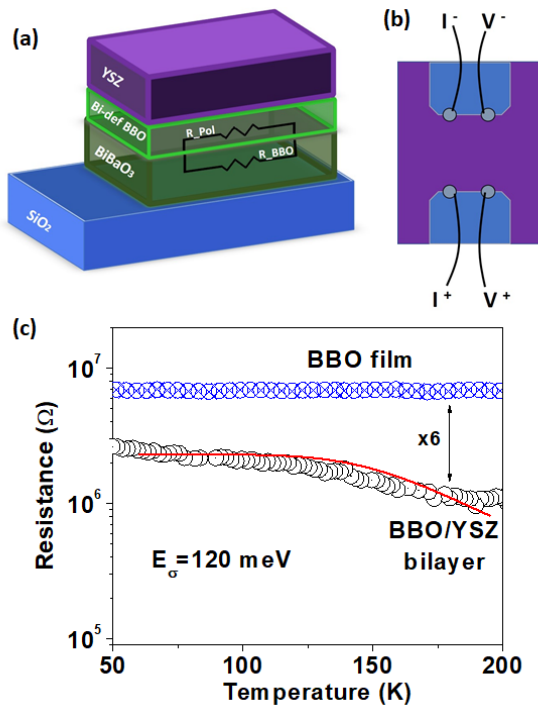


FIG. 2: Sketches showing (a) the $\text{Si}_2/\text{BBO}/\text{Bi-def BBO}/\text{YSZ}$ stack and (b) a top view of the contacted device. Small parts of SiO_2 (top layer of the substrate, blue) were left exposed in order to access the BBO and Bi-deficient BBO layers for 4-points transport measurements. Same colours are used for (a) and (b); (c) 4-points resistance as a function of the temperature recorded for a bare BBO film and a YSZ-capped heterostructure. The red line shows a fitting assuming a polaronic conduction model for the Bi-deficient BBO layer (see text for details).

tain a theoretical value $K_0 \frac{ak_B}{g_d e^2 \nu_0} = 2.5 \Omega/K$, in very good agreement with the fitted value, giving consistency to our analysis.

We recall that it has been theoretically proposed that, upon hole doping, BBO remains insulating due to the coupling between holes and phonons⁴⁶ and the subsequent formation of polarons. This is likely the case of Bi-deficient BBO, where the holes for polaron formation are provided by Bi vacancies, as it will be analyzed in the next section by means of first principles calculations.

III. DFT CALCULATIONS

To study the different physical mechanisms that could trigger the transport properties of Bi-deficient BaBiO_3 , we perform *ab initio* calculations within the framework of Density Functional Theory (DFT) and the projector augmented wave (PAW) method⁴⁷, as implemented in the Vienna *ab initio* package (VASP)^{48,49}. We explicitly treat 10 valence electrons for Ba ($5s^2 5p^6 6s^2$), 15 for Bi ($5d^{10} 6s^2 6p^3$) and 6 for O ($2s^2 2p^4$). To properly

describe the electronic structure of charge ordered and semiconducting BaBiO_3 -specially in the presence of localized defects-, it is necessary to consider long range exchange interactions that are poorly described by the standard local and semilocal functionals as the local density approximation (LDA) or the general gradient approximation (GGA). Therefore, we use the semilocal functionals developed by Perdew, Burke and Ernzerhof (PBE)⁵⁰ and we add the hybrid functional including a fraction of non-local Hartree-Fock exchange interactions through the Heyd-Scuseria-Ernzerhof (HSE06) functionals^{51,52} in all the calculations.

The charge-ordered phase of BaBiO_3 is represented formally by the $\text{Ba}_2^{+2}\text{Bi}^{+3}\text{Bi}^{+5}\text{O}_6^{-2}$ formula unit. The two Bi species are ordered in an alternated way within a monoclinic structure⁵³. To compute the electronic properties of perfect BaBiO_3 and Bi-deficient $\text{BaBi}_{0.75}\text{O}_3$, containing a 25% of Bi-vacancies, we use a supercell rotated 45° with respect to the simple cubic single perovskite and which contains 4 Bi sites in total, 2 per layer and two planes in the z -direction. To explore lower concentrations of Bi-vacancies we also perform calculations in a $2\times 2\times 2$ FCC supercell containing 80 atoms⁶⁰, as the one used in Ref. 46. This larger supercell contains 16 Bi-atoms per unit cell and we account for defect concentrations of 12.5% (2 Bi-vacancies) and 18.75% (3 Bi-vacancies).

The HSE calculations within the smaller unit cell are performed using a 450 eV energy cutoff in the plane waves basis and to evaluate the integrals within the Brillouin Zone (BZ), a $4\times 4\times 3$ Monkhorst-Pack k -point grid is employed. The corresponding values for the energy cutoff and k -points grid in the larger FCC supercell are 400 eV and $2\times 2\times 2$, respectively. The experimental lattice parameters⁵³ are used in all the calculations and internal structural relaxations are performed until the forces on each ion are less than 0.02 eV/Å.

For perfect BaBiO_3 , our calculations predict the semiconducting state with a band gap of 0.90 eV, exhibiting the charge disproportionation between the two different species, Bi^{+3} and Bi^{+5} in agreement with previous calculations⁵⁴. In Figure 3(a) we show the corresponding bandstructure where the full 6s bands of Bi^{+3} are depicted in red and the empty ones of Bi^{+5} are in dark green. It is important to mention that the Bi-O bonds can be described by spatially extended hybridized 6s-2p orbitals and all the bands present a strong s-p hybridization. The color coding used in Figure 3 and in the following ones is just a guide to the eye.

Distinct kinds of defects appear in the presence of Bi vacancies. It is worth to mention that several molecular dynamics steps, followed by relaxation, were necessary to stabilize these defects in order to avoid spurious metallic solutions⁴⁶. In the following, we describe the results obtained for the different Bi vacancies concentrations considered.

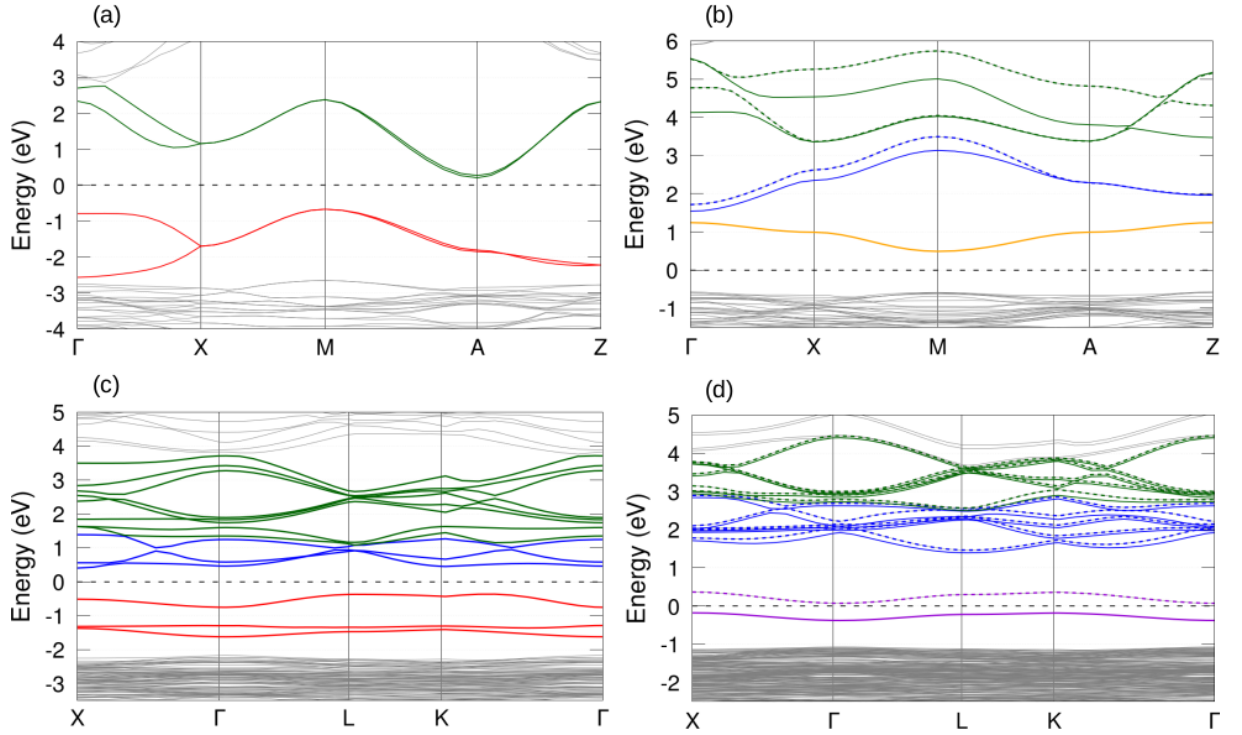


FIG. 3: Spin-polarized band structure of (a) perfect BaBiO₃ and Bi-deficient BaBiO₃ with (b) 25 %, (c) 12.5 % and (d) 18.75 % of Bi-vacancies. Solid lines correspond to spin-up projection and dashed lines to spin-down. In (a) and (c) spin-up and spin-down bands are degenerate. Red bands correspond to Bi⁺³, dark-green ones to original Bi⁺⁵ atoms, and blue to created bipolarons. The orange band in (b) represents the hole trapped at the oxygen cloud centered at the Bi-vacancy sketched in Figure 4 (a) and the violet bands in (d) correspond to the charge/hole polaron originated around Bi₁₂ (see text and Figure 6 (b))

The system with 25 % of Bi vacancy concentration has been simulated in the small cell where one out of four Bi is withdrawn. Independently of the site of the vacancy, whether it is at a Bi⁺⁵ or Bi⁺³ site, the resulting electronic structure is very similar. For instance, if the vacancy is at a Bi⁺⁵ site, in order to compensate the lacking five electrons, each of the remaining two Bi⁺³ liberates two electrons, so that the originally full 6s bands become empty. These two trapped holes at each Bi⁺³ form a bipolaron. Since the remaining Bi⁺⁵ site has its 6s band already empty, the other missing electron turns into a hole trapped at the surrounding oxygen cloud next to the Bi vacancy. On the other way around, if the vacancy is at a Bi⁺³ site, the lacking three electrons give rise to a bipolaron at the remaining Bi⁺³ site and a hole trapped at the oxygen p-bands surrounding the vacancy. In Figure 3 (b) we show the electronic bandstructure, with the orange narrow band corresponding to holes trapped at the oxygen cloud around the vacancy, whose charge density is depicted in Figure 4(a). The bands in blue are the bipolarons with the corresponding charge density shown in Figure 4(b).

As mentioned before, the system with 12.5 % and 18.5 % Bi vacancy concentrations has been simulated with a supercell containing 16 Bi sites. In the case with an even amount of vacancies, the kind of electronic defects are only of the bipolaron type.

In Figure 3 (c), we show the calculated electronic band-structure obtained for the 12.5 % concentration, where there are two vacancies at Bi⁺³ sites in the unit cell. The three occupied bands in red are the full 6s bands of the remaining Bi⁺³, the three bands in blue are those of the bipolarons, and, at higher energies, the eight 6s bands of the Bi⁺⁵ are in dark-green. In the case of even number of vacancies, the system is non-spin polarized so that the bands are doubly degenerate.

When the Bi vacancy concentration is 18.75 %, there are three vacancies in the supercell. For example, if two of the vacancies are at a Bi⁺³ site and the other one at a Bi⁺⁵, there are eleven electrons missing. The six remaining Bi⁺³ sites can provide this charge. That is, five of these Bi⁺³ sites turn into Bi⁺⁵ by trapping two holes each giving rise to five bipolarons (blue bands in Figure 3 (d)). The remaining Bi⁺³ keeps one electron forming a polaron with a localized spin-polarized charge (violet band in Figure 3 (d)).

In order to analyse the role played by each type of defects into the transport properties we proceed to estimate the activated diffusion barrier E_σ in each case.

The hole polaron trapped at the p-bands of the oxygens that surround the Bi vacancy in the highly doped case (25% vacancy concentration), is a mixed type of defect

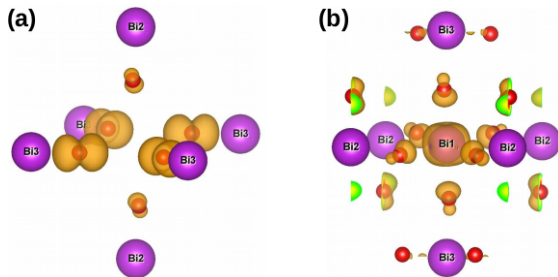


FIG. 4: Charge density plots of Bi-deficient BaBiO₃ with a 25% of Bi-vacancies. Panel (a) shows the hole trapped at the oxygen cloud around the vacancy, corresponding to the orange band depicted in Figure 3 b). The charge density shown in (b) corresponds to the bipolaron at the remaining Bi⁺³ site (blue band in Figure 3 b).

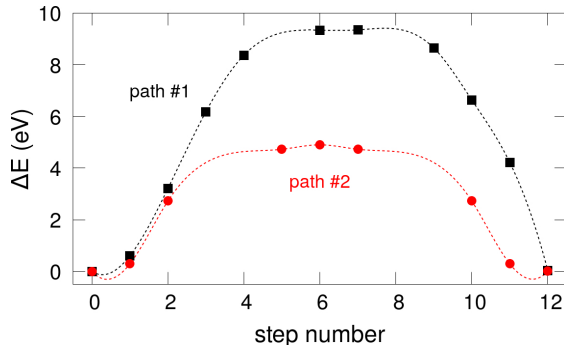


FIG. 5: Activation barrier of the hole polaron trapped at the oxygen *p*-bands that surround the Bi vacancy in the highly doped case, i.e. the 25% concentration of Bi-vacancies. The barrier is calculated using the Nudged elastic bands (NEB,) taking into account two different migration pathways (see text for details).

where the Bi vacancy is bound to a hole electronic cloud. Nudged elastic bands (NEB)⁵⁵ method has been used to estimate the activation barrier, taking into account two different migration pathways. The first one considers the migration of the defect within the *ab*-plane, that is in the plane that contains the part of the hole shared by the 4 in-plane oxygen atoms. The second considered path was with the defect travelling along the (111) – (1̄1̄1) direction, with the inflection point located at an optimized height. That is, the defect travelling from the (1/2, 1/2, 1/2) to the (0, 0, 0) position, through (1/4, 1/4, h_0), being h_0 the optimized distance in the *z*-direction from the *ab*-plane. We obtain $E_\sigma=9.35$ eV and 4.9 eV, respectively. In view of these results, we conclude that the contribution to the electronic conductivity of these type of mixed defects is negligible.

To estimate the maximum of the energy barrier of the polaron and bipolaron trapped at Bi⁺³ sites (violet and blue bands of Figure 3, respectively), we perform a static calculation where the lattice distortion coupled

to the defect is transferred to an intermediate situation that forces the trapped charge to be shared between neighboring Bi sites.

For the case with 18.75 % Bi vacancy concentration, in the top panel of Figure 6 (a), we show the partial density of states (PDOS) projected onto the s-orbitals of two Bi neighboring sites, one of them trapping the polaron (labeled as Bi₁₂) and the other one belongs to a Bi⁺⁵, named Bi₅. The corresponding charge density associated with the polaron is shown in Figure 6 (b). In the bottom panel of Figure 6 (a), we plot the PDOS projected on the same Bi sites but in the situation where the polaron charge is shared in equal parts between them. In Figure 6 (c) we show the related charge density. The energy difference between the initial and the intermediate situation provides an estimation of E_σ , that is 0.54 eV. When this approach is done to estimate E_σ for the bipolaron migration, where now two holes are hopping simultaneously, we obtain $E_\sigma=0.60$ eV.

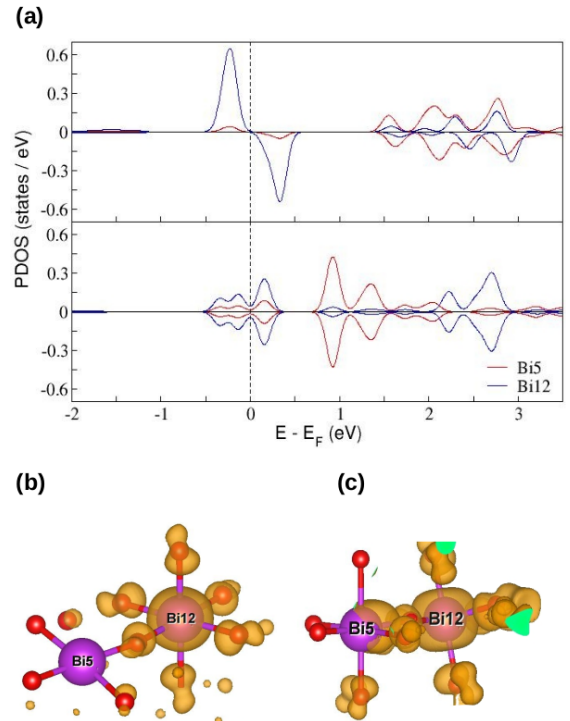


FIG. 6: (a-top panel) PDOS projected onto the *s*-orbitals of two selected Bi atoms, the one with the polaron, i.e. Bi₁₂ and one of its nearest Bi neighbors, i.e. Bi₅; (a-bottom) PDOS projected onto the same Bi atoms for the intermediate situation where the polaronic charge is half-transferred between neighboring sites; (b) Charge-density plot corresponding to the localized state close to E_F shown in the top panel of (a), i.e. the polaron centered at Bi₁₂; (c) Idem (b) after the static perturbation where the polaronic charge is shared with Bi₅.

Interestingly, it is not surprising that this energy scale is related to the electron-phonon coupling in BBO systems, specially with the breathing phonon modes that are

strongly correlated to Bi^{+5} - Bi^{+3} charge ordering. The value around 0.5 eV for E_σ is of the same order of magnitude as the energy shift induced in the electronic bands when frozen phonon perturbations for the breathing mode are performed for bulk BBO⁵⁶. However, as it has been recently reported in Ref. 21, this value decreases to ~ 0.2 eV in confined situations as the one described for the BBO/BaPbO₃ interface. So, it is likely that the value of ~ 0.5 eV obtained for the bulk supercell described here is overestimated since it does not take into account the confinement effects present in the real samples. Therefore, we consider that the actual activation energy might be close to the 0.12 eV obtained from the transport experiments and that the migration of polarons trapped at Bi⁺³ sites plays an important role in the increment of the electrical conductivity with the temperature, experimentally observed in our Bi deficient films.

The existence of polarons or bipolarons trapped at Bi sites in BBO was already theoretically described in Ref. 46. The difference is that in that work the doping is caused by K substitution at Ba sites. They show that local lattice relaxations are sufficiently large to screen the localized holes and that hole doped BBO remains semiconducting upon moderate hole doping. In our work, we show that the level of doping with Bi vacancies is 3 to 5 times larger than with K. Notwithstanding this, it is remarkable that the system remains semiconducting for all the concentrations studied.

IV. CONCLUSIONS

We have shown that it is possible to synthesize thin layers of BBO perovskite with a large amount of Bi-vacancies. Transport properties were modelled with a polaronic model and the existence of these defects was theoretically validated. Our DFT calculations performed for Bi-deficient BBO supercells show that Bi vacancies give rise to different type of polarons, depending on

the vacancies concentration. After the Bi vacancy is formed, the missing electrons induce polaron and/or bipolarons that consist in one or two holes trapped at some of the remaining Bi sites, or even at the oxygen octahedron surrounding the vacancy for large vacancies concentrations.

We conclude that hole doped BBO remains semiconducting despite the large hole concentration induced by the Bi deficiency. We finally estimate the activated diffusion barrier for all these type of defects to analyse their contribution to the transport properties. We show that the calculated energy barriers of the charges trapped at Bi sites are correlated to the electron-phonon coupling energy scale. The calculated activated barriers for the simulated bulk supercells are somewhat larger than the one obtained from the fit of the transport experiments. In view of previous theoretical results for other BBO interfaces, these larger values are expected to decrease in confined situations -such as the Bi-deficient BBO layer studied in this work- and match the experimentally extracted activation energies. We finally conclude that the polarons trapped at Bi sites strongly contribute to the electrical conductivity of Bi-deficient BBO and, in a more general framework, that the control of Bi vacancies can be used as a tool for tuning the electronic properties of this perovskite.

V. ACKNOWLEDGMENTS

The authors received financial support from PICTs 2015-0869, 2016-0867, 2017-1836 and 2019-02128 of ANPCyT, Argentina. Also, funding from EU-H2020-RISE project "MELON" (SEP-2106565560) is acknowledged. DR thanks the Nederlandse Organisatie voor Wetenschappelijk Onderzoek for a visiting grant, project 040.11.735, "Memcapacitive elements for cognitive devices". We thank D. Vega, from CAC-CNEA, for some of the XRD measurements.

-
- ¹ J. Coey, M. Viret, and S. von Molnár, *Advances in Physics* **58**, 571 (2009).
- ² M. Dawber, K. M. Rabe, and J. F. Scott, *Rev. Mod. Phys.* **77**, 1083 (2005).
- ³ C. N. R. Rao, *Ferroelectrics* **102**, 297 (1990).
- ⁴ M. Shellaiah and K. W. Sun, *Chemosensors* **8**, 55 (2020).
- ⁵ A. Sawa, *Materials Today* **11**, 28 (2008).
- ⁶ S. Yu, *Neuro-inspiring computing using resistive synaptic devices* (Springer International Publishing, 2017).
- ⁷ F. Gunkel, D. V. Christensen, Y. Z. Chen, and N. Pryds, *Appl. Phys. Lett.* **116**, 120505 (2020).
- ⁸ M.-A. Rose, B. Šmíd, M. Vorokhta, I. Slipukhina, M. Andrä, H. Bluhm, T. Duchoň, M. Ležaić, S. A. Chambers, R. Dittmann, et al., *Advanced Materials* **33**, 2004132 (2021).
- ⁹ L. F. Mattheiss, E. M. Gyorgy, and D. W. Johnson, *Phys. Rev. B* **37**, 3745 (1988).
- ¹⁰ R. J. Cava, B. Batlogg, J. J. Krajewski, R. Farrow, L. W. Rupp Jr, A. E. White, K. Short, J. F. Peck, and T. Kometani, *Nature* **332**, 814 (1988).
- ¹¹ D. Cox and A. Sleight, *Solid State Communications* **19**, 969 (1976).
- ¹² B. J. Kennedy, C. J. Howard, K. S. Knight, Z. Zhang, and Q. Zhou, *Acta Crystallographica Section B* **62**, 537 (2006).
- ¹³ Z.-X. Shen, P. A. P. Lindberg, B. O. Wells, D. S. Dessau, A. Borg, I. Lindau, W. E. Spicer, W. P. Ellis, G. H. Kwei, K. C. Ott, et al., *Phys. Rev. B* **40**, 6912 (1989).
- ¹⁴ M. Nagoshi, T. Suzuki, Y. Fukuda, K. Ueki, A. Tokiwa, M. Kiruchi, Y. Syono, and M. Tachiki, *Journal of Physics: Condensed Matter* **4**, 5769 (1992).

- ¹⁵ K. Foyevtsova, A. Khazraie, I. Elfimov, and G. A. Sawatzky, Phys. Rev. B **91**, 121114 (2015).
- ¹⁶ N. C. Plumb, D. J. Gawryluk, Y. Wang, Z. Ristić, J. Park, B. Q. Lv, Z. Wang, C. E. Matt, N. Xu, T. Shang, et al., Phys. Rev. Lett. **117**, 037002 (2016).
- ¹⁷ S. Balandeh, R. J. Green, K. Foyevtsova, S. Chi, O. Foyevtsov, F. Li, and G. A. Sawatzky, Phys. Rev. B **96**, 165127 (2017).
- ¹⁸ B. Yan, M. Jansen, and C. Felser, Nature Phys. **9**, 709 (2013).
- ¹⁹ V. Vildosola, F. Güller, and A. M. Llois, Physical Review Letters **110**, 206805 (2013).
- ²⁰ B. Meir, S. Gorol, T. Kopp, and G. Hammerl, Phys. Rev. B **96**, R100507 (2017).
- ²¹ S. Di Napoli, C. Helman, A. M. Llois, and V. Vildosola, arxiv: 2011.08710 (2021).
- ²² T. Makita and H. Abe, Japanese Journal of Applied Physics **36**, L96 (1997).
- ²³ A. Gozar, G. Logvenov, V. Y. Butko, and I. Bozovic, Phys. Rev. B **75**, 201402 (2007).
- ²⁴ K. Inumaru, H. Miyata, and S. Yamanaka, Phys. Rev. B **78**, 132507 (2008).
- ²⁵ H. G. Lee, Y. Kim, S. Hwang, G. Kim, T. D. Kang, M. Kim, M. Kim, and T. W. Noh, APL Materials **4**, 126106 (2016).
- ²⁶ C. Ferreyra, F. Guller, F. Marchini, U. Lüders, C. Albornoz, A. G. Leyva, F. J. Williams, A. M. Llois, V. Vildosola, and D. Rubi, AIP Advances **6**, 065310 (2016).
- ²⁷ C. Ferreyra, F. Marchini, P. Granell, F. Golmar, C. Albornoz, F. Williams, A. Leyva, and D. Rubi, Thin Solid Films **612**, 369 (2016).
- ²⁸ M. Zapf, M. Stübinger, L. Jin, M. Kamp, F. Pfaff, A. Lubk, B. Büchner, M. Sing, and R. Claessen, Applied Physics Letters **112**, 141601 (2018).
- ²⁹ M. Zapf, S. Elsässer, M. Stübinger, P. Scheiderer, J. Geurts, M. Sing, and R. Claessen, Phys. Rev. B **99**, 245308 (2019).
- ³⁰ R. L. Bouwmeester, K. de Hond, N. Gauquelin, J. Verbeeck, G. Koster, and A. Brinkman, physica status solidi (RRL) **13**, 1800679 (2019).
- ³¹ L. Jin, M. Zapf, M. Stübinger, M. Kamp, M. Sing, R. Claessen, and C.-L. Jia, physica status solidi (RRL) **14**, 2000054 (2020).
- ³² G. Kim, M. Neumann, M. Kim, M. D. Le, T. D. Kang, and T. W. Noh, Phys. Rev. Lett. **115**, 226402 (2015).
- ³³ S. J. Skinner and J. A. Kilner, Materials Today **6**, 30 (2003).
- ³⁴ M. Kilo, G. Borchardt, B. Lesage, O. Kaitasov, S. Weber, and S. Scherrer, Journal of the European Ceramic Society **20**, 2069 (2000).
- ³⁵ See Supplemental Material at (link) for additional X-ray diffraction and TEM experiments (????).
- ³⁶ D. J. Keeble, S. Wicklein, L. Jin, C. L. Jia, W. Egger, and R. Dittmann, Phys. Rev. B **87**, 195409 (2013).
- ³⁷ C. M. Brooks, R. B. Wilson, A. Schäfer, J. A. Mundy, M. E. Holtz, D. A. Muller, J. Schubert, D. G. Cahill, and D. G. Schlom, Applied Physics Letters **107**, 051902 (2015).
- ³⁸ M. D. Scafetta and S. J. May, Phys. Chem. Chem. Phys. **19**, 10371 (2017).
- ³⁹ F. Li, B. A. Davidson, R. Sutarto, H. Shin, C. Liu, I. Elfimov, K. Foyevtsova, F. He, G. A. Sawatzky, and K. Zou, Phys. Rev. Materials **3**, 100802 (2019).
- ⁴⁰ A. W. Sleight, Phys. C **514**, 152 (2015).
- ⁴¹ A. Prakash, P. Xu, A. Faghaninia, S. Shukla, J. W. Ager, C. S. Lo, and B. Jalan, Nature Commun. **8**, 15167 (2016).
- ⁴² T. Zhao, W. Shi, J. Xi, D. Wang, and Z. Shuai, Sci. Reports **6**, 19968 (2016).
- ⁴³ R. T. Dolloff, Journal of Applied Physics **27**, 1418 (1956).
- ⁴⁴ M. Jaime, H. T. Hardner, M. B. Salamon, M. Rubinstein, P. Dorsey, and D. Emin, Phys. Rev. Lett. **78**, 951 (1997).
- ⁴⁵ S. Sugai, S. Uchida, K. Kitazawa, S. Tanaka, and A. Katsumi, Phys. Rev. Lett. **55**, 426 (1985).
- ⁴⁶ C. Franchini, G. Kresse, and R. Podloucky, Phys. Rev. Lett. **102**, 256402 (2009).
- ⁴⁷ P. Blöchl, Phys. Rev. B **50**, 17953 (1994).
- ⁴⁸ G. Kresse and J. Furthmüller, Phys. Rev. B **54**, 11169 (1996).
- ⁴⁹ G. Kresse and D. Joubert, Phys. Rev. B **59**, 1758 (1999).
- ⁵⁰ J. Perdew, S. Burke, and M. E. M, Phys. Rev. Lett. **77**, 3865 (1996).
- ⁵¹ J. Heyd, G. E. Scuseria, and M. Ernzerhof, The Journal of Chemical Physics **118**, 8207 (2003).
- ⁵² A. V. Kruckau, O. A. Vydriv, A. F. Izmaylov, and G. E. Scuseria, The Journal of Chemical Physics **125**, 224106 (2006).
- ⁵³ D. Cox and A. Sleight, Solid State Communications **19**, 969 (1976).
- ⁵⁴ C. Franchini, A. Sanna, M. Marsman, and G. Kresse, Phys. Rev. B **81**, 085213 (2010).
- ⁵⁵ G. Henkelman and H. Jónsson, J. Chem. Phys. **113**, 9901 (2000).
- ⁵⁶ Z. P. Yin, A. Kutepov, and G. Kotliar, Physical Review X **3** (2013).
- ⁵⁷ R. J. D. Tilley, *Defects in solids* (John Wiley Sons, Inc, 2008).
- ⁵⁸ $g_d = Nca^3$, where N is the available sites for a jump, c is the defect concentration and a was defined in the text. See for instance Ref. 57.
- ⁵⁹ $g_d = 3/8$ taking N equal to 6 and c is estimated considering 1 polaron in the supercell of volume $(4a)^3/4$.
- ⁶⁰ To build this FCC supercell we begin with a 2x2x2 supercell of the simple cubic perovskite containing 40 atoms in total and we perform several molecular dynamics steps, followed by relaxation, to stabilize the breathing distortion driven by the charge disproportionation. Once this distortion agree well with the experimental one, we build up again a 2x2x2 supercell, described within the FCC Bravais lattice.